Journal of Materials Chemistry C

Accepted Manuscript

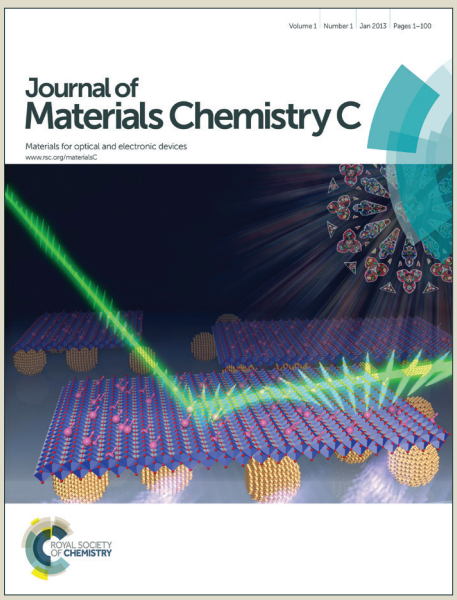

ROYAL SOCIETY OF CHEMISTRY

www.rsc.org/materialsC

Revealing the Role of Cationic Displacement in Potassium-Sodium Niobate Lead-free Piezoceramics by adding W^{6+} ions

L. Ramajo[1,†], M. Castro[1], A. del Campo[2], J. F. Fernandez[2], F. Rubio-Marcos[2, †,*]

[1]Instituto de Investigaciones en Ciencia y Tecnología de Materiales (INTEMA), Av. Juan B Justo 4302 (B7608FDQ), Mar del Plata, Argentina.

[2]Electroceramic Department, Instituto de Cerámica y Vidrio, CSIC, Kelsen 5, 28049, Madrid, Spain.

*Author to whom correspondence should be addressed. Phone: +34 91 735 58 40 Fax: +34 91 735 58 43. Email: frmarcos@icv.csic.es

† **Author Contributions:** L. Ramajo and F. Rubio-Marcos contributed equally.

Abstract

The effect of the structural modifications induced by the replacement of the B sites with W^{6+} ions in $(K_{0.44}Na_{0.52}Li_{0.04})[(Nb_{0.86}Ta_{0.10}Sb_{0.04})_{1-x}W_{5x/6}]O_3$ lead free ceramics is investigated. Here we show the coexistence between a tetragonal symmetry (**T**) and an orthorhombic symmetry (**O**) onto the perovskite structure, which is tuned by varying the doping level. In addition, this polymorphic behaviour is accompanied by the appearance of a secondary phase, which can be detected through XRD and Raman results. A correlation between the presence of both structural features and the W^{6+} content has been evaluated, and therefore this lead free system reveals a transition from a normal ferroelectric to a 'relaxor-like' ferroelectric due to the cation disorder in the perovskite-structure in doped samples. A large diffusivity value (γ) has been attained when the *x* value reached 0.05 owing to the involved **O-T** polymorphic phase, as well as by the appearance of a secondary phase. The experimental proofs make clear that the role of the secondary phase is to capture the alkali ions of (KNa)NbO_3-based system, provoking a cation disorder in the perovskite-structure matrix. The significance of this work lies in evaluating whether such a material can benefit the understanding of (KNa)NbO_3-based ceramics and the expanding of their applications range.

KEYWORDS: *Lead- free materials; Potassium-Sodium Niobate phase; Piezoelectric ceramics*

1. Introduction

Lead titanate-zirconate ceramics ($Pb(Ti,Zr)O_3$ - PZT) are the most widely used piezoelectric ceramics, on account of their high piezoelectric properties response, large-scale production capability and the tailoring of their properties through composition. However, due to the toxicity of lead, a wide range of regulations concerning environmental preservation are increasingly being introduced worldwide[1-2]. PZT ceramics are still allowed because of the lack of an adequate alternative. Among the available lead-free ferroelectric ceramics, one promising candidate is the family of sodium potassium niobate $(K,Na)NbO_3$ (KNN), on account of its good electromechanical properties[3-5]. As for PZT, the sinterability of KNN-based materials can be improved by using different sintering aids and dopants [6-9].

Numerous studies on lead-free piezoelectric ceramics such as $(K,Na)NbO_3$, $BaTiO_3$-based, Bi-layered, bismuth sodium titanate and tungsten bronze-type materials have been recently published [10-12]. In this way, niobates $(K,Na)NbO_3$ (KNN)-based ceramics have showed good piezoelectric and electric properties, high Curie temperature and environmental inequity. *Dai et al.*[13] investigated the influence of the morphotropic phase boundary and electrical properties of $K_{1-x}Na_xNbO_3$ ceramics with x=0.48–0.54 prepared by a conventional solid-state reaction method. They found that a typical morphotropic phase boundary exists at x=0.52–0.525, separating the monoclinic and orthorhombic phases. Moreover, the sample with the composition near x=0.52 showed the maximum value of the piezoelectric constant (d_{33}=160 pC/N).[13]

Saito et al. reported exceptionally high piezoelectric properties in the system $(K,Na)NbO_3$–$LiTaO_3$–$LiSbO_3$[14]. This study was based on chemical modifications, in the vicinity of the MPB of $(K,Na)NbO_3$ (KNN), by complex simultaneous substitutions in the A (Li) and B (Ta and Sb) site of the perovskite lattice. Besides these chemical modifications, they developed a novel processing route for producing textured polycrystals of the KNN-based compositions by additional engineering of the microstructural design. However, the compositional inhomogeneity, particularly the inhomogeneous distribution of Nb, Ta and Sb on the B-site of the perovskite lattice, is rather difficult to be avoided due to the phase segregation of end members over a wide temperature interval[15]. In addition, apparent compositional segregation in KNN has been evidenced in ceramics annealed for a long time[16].

Recently, we have reported in the $(K,Na,Li)(Nb,Ta,Sb)O_3$ system (abbreviated as KNL-NTS), that the dielectric, piezoelectric and elastic material responses are fundamentally related to extrinsic effects.[17] Nonetheless, the dielectric and mechanical losses at room temperature are similar to those of a soft PZT ceramic and too high to be used in power devices. Thus, these materials need to be modified by the use of suitable dopants, like for “pure” KNN. The effect of doping on various physical and chemical properties of this material is considered as a classic story in the field of piezoelectric materials, which are used to modify the crystal structure and the piezoelectricity of these systems. Many aliovalent compositional

modifications to KNN-based system have been studied either with higher valence substitutions (donors), or with lower valence ions (acceptors).

There are few reports available with WO_3 incorporation in KNN-based ceramic. *Zang et al.* [18] synthesized lead-free $(K_{0.48}Na_{0.52})(W_{2/3}Bi_{1/3})_xNb_{1-x}O_3$ (KNN-WBi) piezoceramics with x ranging from 0.004 to 0.010 by conventional ceramic processing. The sintered ceramics showed the perovskite structure without detectable secondary phase containing W and Bi. With increasing x, the orthorhombic-tetragonal phase transition temperature (T_{O-T}) decreased from 200 to 184 °C whereas, the tetragonal-cubic phase transition temperature (T_C) decreased slightly. With the doping of ($W_{2/3}Bi_{1/3}$), the piezoelectric properties were greatly improved and the piezoelectric constant exhibited a maximum value of 136 pC/N, at x=0.008. *Rani et al.*[19] reported the effect of WO_3 addition on electrical and optical properties of $(K_{0.17}Na_{0.83})NbO_3$. They established that WO_3 addition causes the increase in the volume of unit cell of $(K_{0.17}Na_{0.83})NbO_3$ ceramic and promotes densification. The value of dielectric constant at room temperature and at Curie temperature was found to be increasing with increasing WO_3 concentration and it was found to be maximum for x = 5 wt. % WO_3.

In the present work, W^{6+} is selected as the dopant of KNL-NTS ceramics. Thus, on the basis of ionic radii,[20] the W^{6+} ion (r_w^{6+}: 0.60 Å for a coordination number CN = 6) falls in the size range of B-site position (r_{Nb}^{5+}: 0.64 Å, r_{Ta}^{5+}: 0.64 Å, r_{Sb}^{5+}: 0.60 Å CN = 6). Considering its valency, W^{6+} can act as a donor-dopant if introduced in B-site. Such behaviours may cause several effects on the dielectric behaviour through interaction with perovskite structure. Therefore, in order to introduce the W^{6+} ion into the B-site of the perovskite lattice, we selected B-site deficiency, with a global formula $(K_{0.44}Na_{0.52}Li_{0.04})[(Nb_{0.86}Ta_{0.10}Sb_{0.04})_{1-x}W_{5x/6}]O_3$, hereafter abbreviated as KNL−$(NTS)_{1-x}W_{5x/6}$. We synthesized the $(K,Na)NbO_3$–$LiTaO_3$–$LiSbO_3$ system, replacing the B-sites with W^{6+} ions [KNL−$(NTS)_{1-x}W_{5x/6}$], that has a polymorphic behaviour between a tetragonal symmetry and an orthorhombic symmetry. The substitution in the B (Nb^{+5}, Ta^{+5} and Sb^{+5}) sites of the perovskite lattice resulted in the presence of a new secondary phase, which modifies the phase transitions of the system. These structural changes find their explanation due to the partial retention of the alkali elements involved in $(KNa)NbO_3$-based perovskite structure, which move to form the secondary phase. The main achievement is related to the tuning of the ferroelectric behaviour, which evolves from a normal ferroelectric to a 'relaxor-like' ferroelectric because of the heterogeneous distribution of the W^{6+} ions.

2. Experimental details

Sample preparation: The $(K_{0.44}Na_{0.52}Li_{0.04})[(Nb_{0.86}Ta_{0.10}Sb_{0.04})_{1-x}W_{5x/6}]O_3$ composition was prepared by the conventional ceramic processing route. Na_2CO_3, Li_2CO_3 (Panreac, 99.5%), K_2CO_3 (Merck, 99%), WO_3, Nb_2O_5, Ta_2O_5, and Sb_2O_5 (Sigma–Aldrich, ≥ 99.5%, 99.9%, 99% and 99.995%, respectively) were used as starting raw materials. They were individually milled, in order to obtain an appropriate distribution of the particle size.

Powders with different WO_3 concentrations (x = 0, 0.005, 0.010, 0.030 and 0.050), abbreviated as KNL−$(NTS)_{1-x}W_{5x/6}$, were weighted by electronic balance and ball milled for 3 h in ethanol medium in a high energy laboratory ball-mill with zirconia balls. Afterwards, the resulting powders were dried and calcined at 700 ºC for 2 h at 3 ºC/min. These calcined powders were attrition milled again and pressed at 200 MPa into disks of 10 mm in diameter and 0.7 mm thick. The pellets were finally sintered in air at 1125 ºC for 2 h. Bulk densities of the samples were determined using the Archimedes method.

X-ray Diffraction (XRD): Crystalline phases were characterized by X-ray diffraction (XRD) (D8 Advance, Bruker, Germany), using CuK_α radiation, on powders obtained by milling the sintered ceramics. The patterns were recorded over the angular range 5–70° (2θ) with a step size of 0.0334° and a time per step of 100 seconds, using Cu Kα radiation (λ = 0.154056 nm) with working voltage and current of 40 kV and 100 mA, respectively. Peak positions were fit assuming a Lorentz peak shape.

Atomic Force Microscopy and Confocal Raman Microscope mapping. The experiments were performed using a Confocal Raman Microscope (CRM) coupled with Atomic Force Microscopy (AFM, Witec alpha-300R). The sample was imaged in AFM AC Mode using ArrowFM cantilevers (Nanoworld, Germany) with a resonance frequency in the range of 70–90 kHz and damping of r = 50%, recording both topography and phase images simultaneously. Raman spectra were obtained using a frequency-doubled NdYAG laser operating at 532 nm and a 100X objective lens (NA = 0.9). The incident laser power was 20 mW. The optical diffraction resolution of the Confocal Microscope was limited to about ~250 nm laterally and ~500 nm vertically. Raman spectral resolution of the system was down to 0.02 cm^{-1}. The microscopy sample was mounted on a piezo-driven scan platform having 4 nm lateral and 0.5 mm vertical positional accuracy. The piezoelectric scanning table allows steps of 3 nanometres (0.3 nm in the vertical direction), giving a very high spatial resolution for both the AFM and the Confocal Raman Microscopy. The microscope base was also fitted with an active vibration isolation system, active 0.7–1000 Hz. Collected spectra were analysed by using Witec Control Plus Software, and Raman mode positions were fit assuming a Lorentz peak shape.

Electron Microscopy: Microstructure was evaluated on polished and thermally etched samples (1000ºC for 5min) using a Field Emission Scanning Electron Microscope, FE-SEM (Hitachi S-4700). The composition of the ceramics was estimated using Energy Dispersive Spectroscopy, EDS.

Electrical Properties: For the electrical measurements, silver paste electrodes were coated on both sides of the sintered samples. After fired at 700 ^oC for 20 minutes, these disks can be used for characterizing electrical performance. In order to test the piezoelectric constant, the samples were polarized under a direct current (dc) electric field of 40 kV/cm in a silicone oil bath at 25 ºC for 30 min. The piezoelectric constant d_{33} was measured using a piezo d_{33} meter (YE2730A d_{33} METER,

APC International, Ltd., USA). Dielectric properties were determined at different temperature and frequencies using an impedance analyzer HP4294A in the frequency range 100 Hz to 1 MHz.

3. Results

3.1. Structural characterization of the KNL−$(NTS)_{1-x}W_{5x/6}$ ceramics by XRD: Identification of the polymorphic behaviour.

Figure 1 presents the X-ray diffraction patterns of KNL−$(NTS)_{1-x}W_{5x/6}$ ceramics for different W^{6+} amounts and sintered at 1125 °C for 2 hours. The diffraction patterns correspond to a perovskite structure. Furthermore, doped-samples present the same main perovskite phase and a minor secondary phase, which is assigned to $K_6LiNb_6O_{17}$ (PDF# 36-0533) or $K_6Nb_{10.88}O_{30}$ (PDF# 87-1856), with tetragonal tungsten-bronze phase structure (TTB).[21-22] This phase is more relevant in high doped ceramics, indicating that W^{6+} concentration affects the formation of secondary phases.

The **inserts** of the **Figure 1** displays the splitting of the (200) pseudo-cubic peak into (200) and (002), which suggests a non-cubic symmetry in these samples. The inserts show a detail of the XRD diffraction pattern in the 2θ range 44.5º to 46.5º of the KNL−$(NTS)_{1-x}W_{5x/6}$ ceramic system. Moreover, as represented in the inserts, the W^{6+} doping produces changes on the symmetry of the perovskite structure. All samples display this splitting associated with the coexistence between a tetragonal symmetry, **T**, and an orthorhombic symmetry, **O**, (see insert of the **Figure 1**). The coexistence of different polymorphs (tetragonal and orthorhombic phases), was previously reported on KNL-NTS bulk ceramics.[23-26] It is well known that the tetragonal symmetry, **T**, of the perovskite phase can be deconvoluted in two Lorentzian peaks, $(002)_{\mathbf{T}}$, and $(200)_{\mathbf{T}}$. In addition, in these samples two peaks located at ~45.4 and ~45.6º (2θ) which are associated with the orthorhombic symmetry, **O**, are detected. At low W^{6+} contents ($x \leq 0.01$), the peaks associated with tetragonal symmetry are more relevant than in the ceramics with high W^{6+} contents ($x \geq 0.03$), which implies a stabilization of tetragonal symmetry at low W^{6+} concentrations (see insert of the **Fig. 1**). As a consequence, the most probable origin of this behaviour must be related to the solubility of W^{6+} ions in the perovskite structure, and therefore with the chemical homogeneity of the system. So, we suppose that the perovskite lattice cannot accommodate the nominal W^{6+} content since it corresponds to B-site excess. Thus, the corresponding excess should be directly compensated by the eviction of some Nb^{5+} ions, with the transformation of the perovskite structure towards an orthorhombic symmetry, and the apparition of the secondary phase.

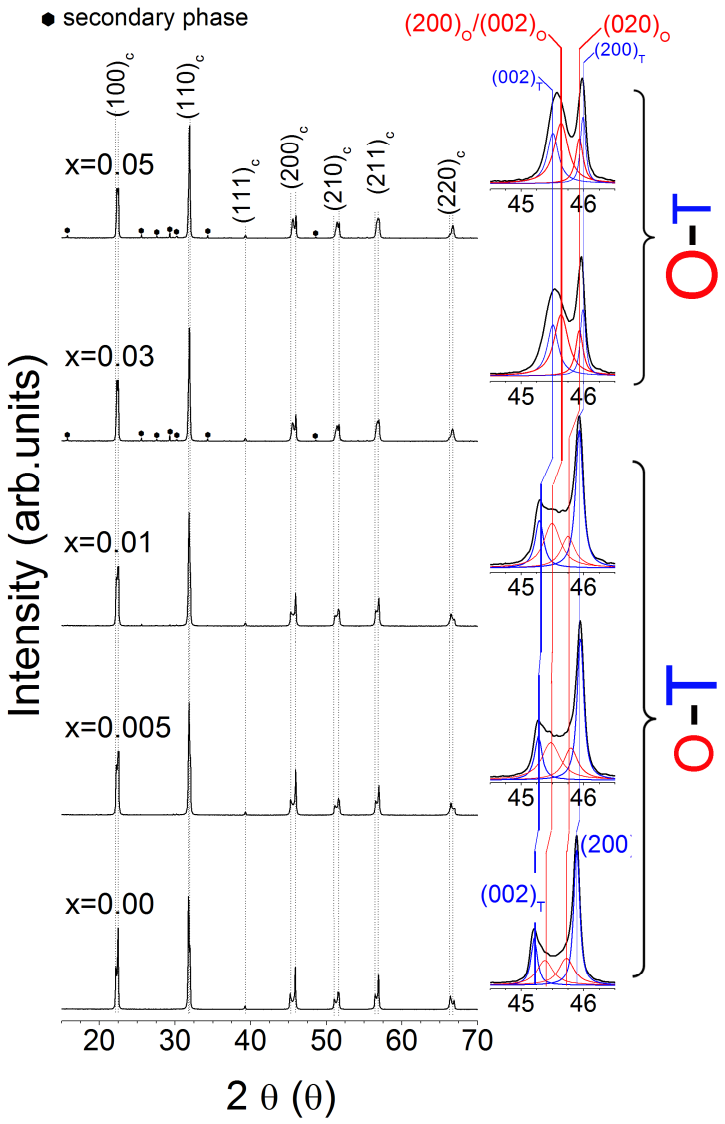

Figure 1. *Influence of the W^{6+} concentration in the crystalline structure of the KNL−(NTS)$_{1-x}$W$_{5x/6}$ ceramic:* The figure shows X-ray diffraction patterns of KNL−(NTS)$_{1-x}$W$_{5x/6}$ ceramics sintered at 1125 ºC for 2h. In the ceramics with high W^{6+} content ($x \geq 0.03$) appears different peaks that are associated with the occurrence of the secondary phase and is signaled with a circle symbol. The **inserts** of each figure show a detail of the XRD diffraction pattern in the 2θ range 44.5º to 46.5º of the KNL−(NTS)$_{1-x}$W$_{5x/6}$ ceramics. These patterns are fitted to the sum of four Lorentzian peaks, which are indexed as 2 tetragonal peaks (in blue colour) plus 2 orthorhombic peaks (in red colour) of the perovskite phase. (T: Tetragonal symmetry and O: orthorhombic symmetry)

3.2. Study of the secondary phase location using Raman imaging.

To verify that the crystalline symmetry and the appearance of the secondary phase are influenced by the doping on the KNN-based system, additional experiments were performed by confocal Raman microscopy (CRM). According to the nuclear site group analysis, Raman active modes of the tetragonal *P*4*mm* (C_{4v}^1) crystal symmetry are associated to the BO^{6-} perovskite octahedron.[27-28] So, the vibrations of the BO^{6-} octahedron consist of $1A_{1g}$ (υ_1) + $1E_g$ (υ_2) + $2F_{1u}$ (υ_3, υ_4) + F_{2g} (υ_5) + F_{2u} (υ_6). From these vibrations, $1A_{1g}$ (υ_1) + $1E_g$ (υ_2) + $1F_{1u}$ (υ_3) are stretching modes and the other ones bending modes. In particular, A_{1g} (υ_1) and F_{2g} (υ_5) have been detected as being relatively strong scatterings in systems similar to the one studied in this

paper due to a near-perfect equilateral octahedral symmetry. The presence of the main vibration modes of the NbO_6^- octahedron as shown in **Fig. 2(a)** is another evidence of the formation of perovskite structure, which corresponds to the red regions marked in the **Fig. 2(b-f)**. Clear differences can be observed in the shape of the spectra as a function of doping amount, particularly in the 500 to 700 cm^{-1} region. The details of the Raman modes of the perovskite are magnified in connecting inserts in **Fig. 2a**, which can be assigned to E_g (υ_2) and A_{1g} (υ_1) Raman modes, respectively. The evolution of the A_{1g} mode shows a continuous Raman red-shift of this mode when the *x* increases, see **inserts of the Fig. 2(a)**. So, from **insert** in top of the **Fig. 2(a)** shows an enlargement of the Raman modes A_{1g} (υ_1) and E_g (υ_2), exhibiting a Raman red-shift of 8.1 cm^{-1} for $x = 0.05$ with respect to the undoped ceramics. Thus, one can deduce that the incorporation of W^{6+} into the perovskite lattice slightly alters the observed vibration frequencies, shifting the A_{1g} (υ_1) mode to lower wavenumber due to a decrease in the strength constant force, caused by the lengthening of the distance between B^{5+} type ions and their coordinated oxygens.

A careful examination of the Raman spectra, **Figure S1,** reveals the presence of Raman modes corresponding to KNN-based phase and the appearance of an additional Raman peak. This new Raman peak is attributed to the appearance of a characteristic Raman mode of the TTB secondary phase at ~ 690 cm^{-1},[29] [blue regions marked in the **Fig. 2(c-f)]**, which emerges concomitantly with the *x* increases *(more information about this secondary phase in **Supporting Information 1**)*. **Fig. 2(b-f)** shows a sequential series of the Raman maps in which we can observe and quantify the KNN-based phase (marked in red) and TTB secondary phase distribution (marked in blue) into ceramics as a function of the W^{+6} content. As mentioned above, the average Raman spectrum of the secondary phase can be indexed on the basis of a phase mixture constituted by a majority of KNN-based phase and a minority of secondary phase, see ***Supporting Information 1***.

As a result, it can be observed that the secondary phase amount increases with the W^{6+} concentration, **Fig. 2(g)**, while changes in the Raman shift of Raman modes associated to the BO_6^- octahedron, **Fig. 2(a),** allow determining variations in polarization, which are associated with modifications of the constant force of the octahedron due to deformation or stress.[30-31] The last phenomenon (polarization changes) must be associated with the evolution of polymorphic behaviour observed by XRD.

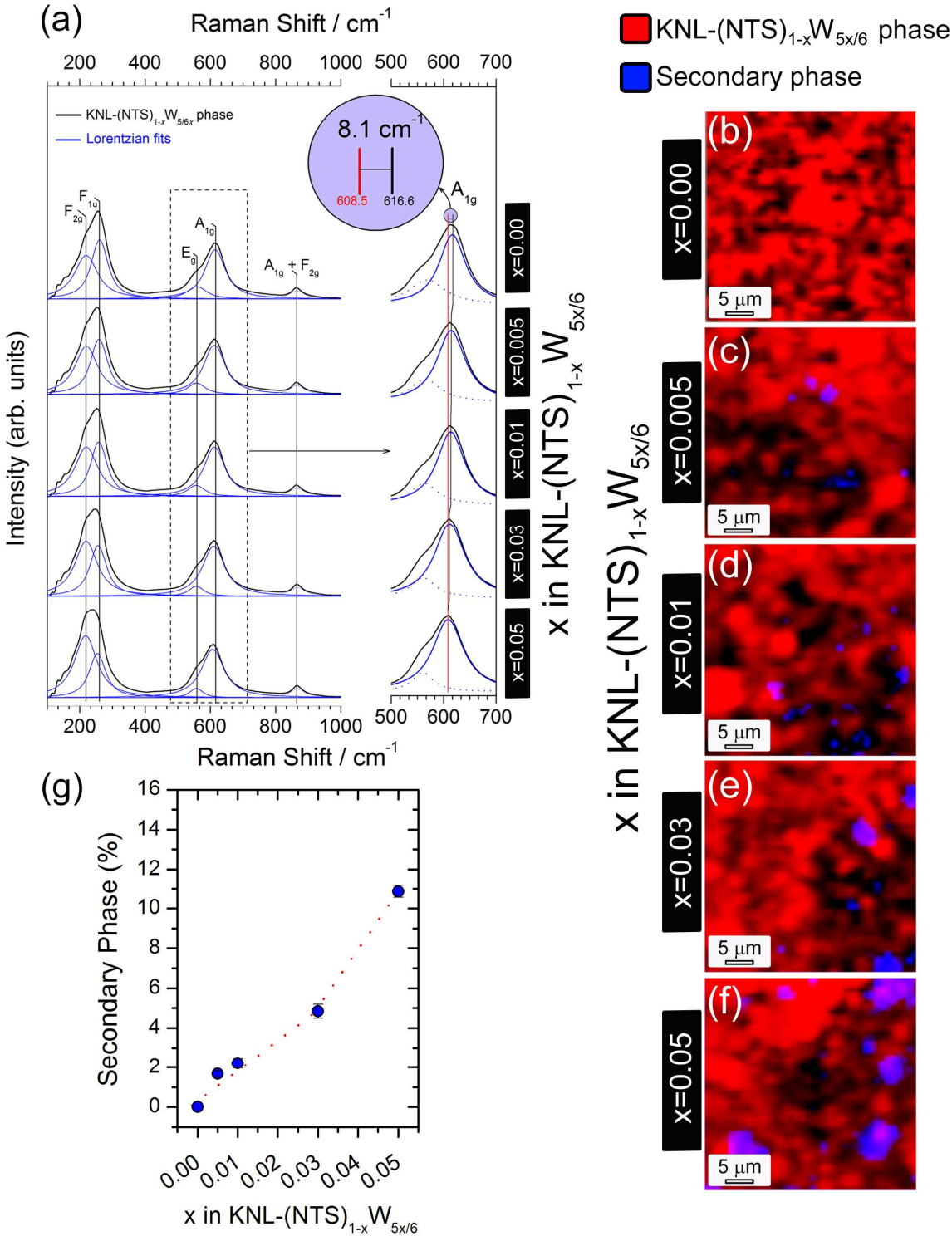

Figure 2. *Detection of the secondary phase observed in the KNL-NTS ceramics doped with different W^{6+} amounts:* **(a)** Average Raman spectra of ceramics. These Raman spectra are fitted to the sum of two Lorentzian peaks, ascribed to the E_g (υ_2), A_{1g} (υ_1) corresponding to Raman modes of the KNL-NTS perovskite phase. Moreover, the insert in top of the Fig. (a) shows an enlargement of the Raman shift taken between the ceramics with *x*=0.00 and x=0.05, exhibiting an increased Raman shift of 8.1 cm^{-1}. **Fig. b to f** Raman image of ceramics with different W^{6+} amounts, exhibiting the secondary phase location, blue areas. The Raman image is derived by summing the total spectral pixel intensity from 150 cm^{-1} to 1000 cm^{-1}. The secondary phases signalled in regions with blue colours, whereas the modified KNN perovskite phase corresponds to red regions. **(g)** Evolution of the secondary phase concentration obtained from the Raman Spectroscopy as a function of W^{6+} content. In addition, the reader can find more information about this secondary phase in ***Supporting Information 1***.

3.3. Determination of the secondary phase composition.

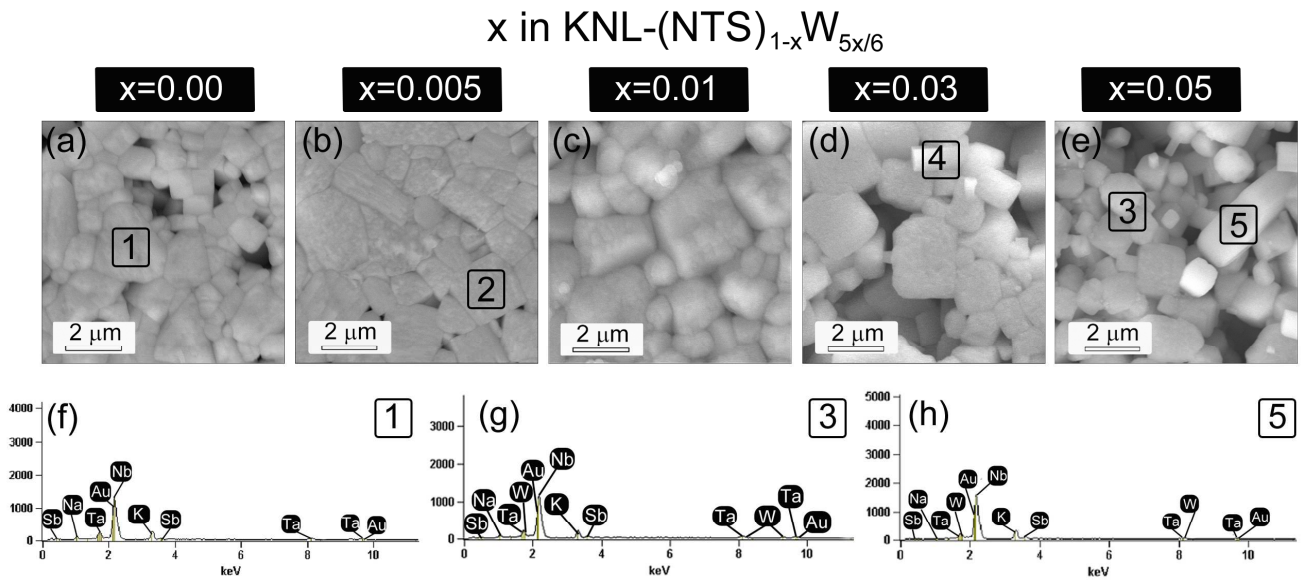

	O	Na	K	Li	Nb	Ta	Sb	W	Na/K
Point 1	61.2	9.5	8.0	---	18.5	2.0	0.8	---	1.19
Point 2	60.2	10.3	9.2	---	17.7	1.8	0.6	0.2	1.12
Point 3	62.7	7.8	7.0	---	18.2	2.5	1.2	0.6	1.11
KNL-NTS nominally composition	60.0	10.4	8.8	0.8	17.2	2.0	0.8	---	1.18
Point 4	62.9	4.8	9.7	---	20.3	1.2	0.9	0.2	0.49
Point 5	64.3	3.4	8.7	---	20.8	1.6	0.8	0.4	0.39
TTB [29] $Li_x(K_{0.78}Na_{0.22})_6(Nb_{0.86}Ta_{0.10}Sb_{0.04})_{10.9}O_{30}$	64.0	2.8	10.0	---	20.0	2.3	0.9	---	0.28

Figure 3. SEM images of KNL−$(NTS)_{1-x}W_{5x/6}$. (**a**) undoped; (**b**) $x = 0.005$ (**c**) $x = 0.01$; and (**d**) $x = 0.03$, (**e**) $x = 0.05$; and energy dispersive spectra (EDS) at five different regions (**1-5**) of KNL−$(NTS)_{1-x}W_{5x/6}$ with x between 0.00 to 0.05. The table presents the composition on the points shown on micrograph derived from EDS spectra. The table represents the atomic percentages of elements.

The FE-SEM micrographs of the KNL−$(NTS)_{1-x}W_{5x/6}$ ceramics with x between 0.00 to 0.05 are shown in **Figure 3**(**a**–**e**). The microstructure of undoped materials consisted in homogeneously cubic-shaped grains with an average equivalent diameter of ~1 μm. These ceramics present a porous microstructure without secondary phases. The addition of a low amount of the W^{6+} produces an inhomogeneous grain growth and a reduction in the porosity level (see **Table 1**). A change in the average grain size and the grain morphology is observed with the W^{6+} content, as depicted in **Figs. 3**(**d-e**). In addition, for higher W^{6+} content ($x \geq 0.03$) a secondary re-crystallization appears forming small plate-like grains, see **Fig. 3(d-e)**. According to XRD results, secondary phases are observed and their amount increased with the doping level. Additionally, the appearance of secondary amorphous phase is associated with the transitory liquid phase that assisted sintering process. This liquid phase has been also already observed in undoped samples only for the short sintering time.[32] In this work, the liquid phase is

stabilized for low doping content. The presence of W^{6+} ions enhances probably the amount of transient liquid phase and thus the grain growth is promoted.

EDS analysis was carried out on all the specimens in order to identify the composition of the TTB phase. **Figs. 3(f-h)** illustrate the EDS a spectrum corresponding to the matrix and TTB phase, respectively, and the composition analysis is also summarized in the included table. Na, K, Nb, Sb, W and Ta ions were found in the matrix and its composition is confirmed to be the very close to KNL−NTS, see composition table of the **Fig. 3** derived from EDS spectra. In the TTB phase, however, a low relation Na/K has been expected, see composition table of the **Fig. 3.** Through the EDS analysis, the composition of the secondary phase is close to the $K_6Nb_{10.88}O_{30}$-based phase with tetragonal tungsten-bronze structure.

3.4. Influence of the Structural and Microstructural changes on the Functional Properties of the $KNL-(NTS)_{1-x}W_{5x/6}$ ceramics.

Table 1. Density (ρ), relative density (ρ_r), dielectric properties (ε', tan δ), and piezoelectric constant (d_{33}) of $KNL-(NTS)_{1-x}W_{5x/6}$ ceramics sintered at 1125 ºC for 2 h. *The ρ and d_{33} values are the average values of five specimens. Data are measured at 25°C and 24 hours after poling. Theoretical density 4.69 g/cm³ [21]*

$KNL-(NTS)_{1-x}W_{5x/6}$ (x)	ρ (g/cm³)	ρ_r (%)	ε'	*tan*(δ)	d_{33} (pC/N)
0.000	4.41±0.024	94.1	880	0.007	230
0.005	4.53±0.043	96.6	861	0.025	195
0.010	4.50±0.022	96.0	664	0.037	180
0.030	4.28±0.028	91.3	566	0.059	140
0.050	4.26±0.037	90.8	529	0.062	95

Table 1 shows density, real part (ε') of dielectric permittivity, dielectric loss (tanδ) and piezoelectric constant of sintered samples. It can be observed that the ceramics with $0.005 \leq x \leq 0.01$ show higher density values than pure KNL-NTS ceramics, although a diminution in ε'and d_{33} values has been observed when the doping level increases. This behaviour can be attributed to the secondary phase formation, the density diminution, and the coexistence of different polymorphic phases. Moreover, the presence of the secondary phase correlates with the higher dielectric losses.

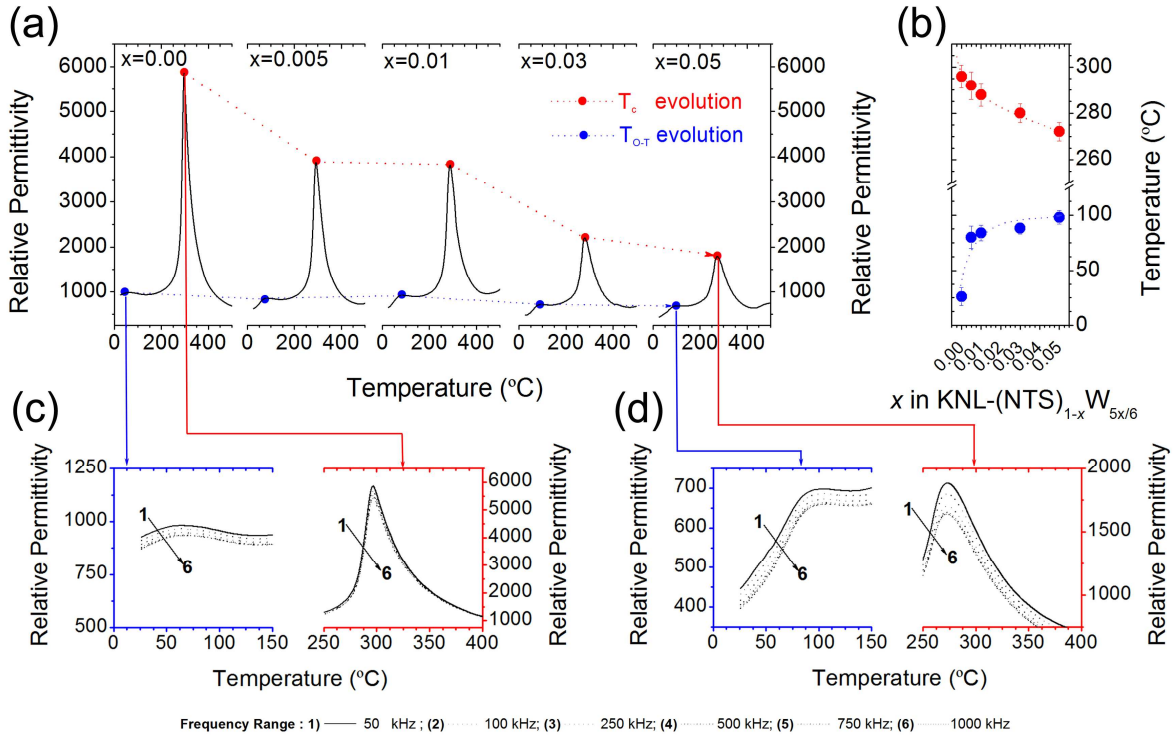

Figure 4. (a) Real permittivity (ε´) as a function of temperature of KNL−$(NTS)_{1-x}W_{5x/6}$ sintered ceramics (at 50 kHz). The part **(b)** shows the evolution of the T_c and the phase transition temperatures from orthorhombic to tetragonal phase (T_{O-T}) of the KNL−$(NTS)_{1-x}W_{5x/6}$ ceramics with different content in W^{6+} (the sensitivity of the phase transition temperatures, T_{O-T} and Tc, were estimated on ±5 ºC). The parts **(c-d)** show the temperature dependence of ε_r for the undoped ceramic (c) and the ceramic with $x = 0.05$ (d) as a function of frequency, in which are shown the T_{O-T} (marked in blue colour) and T_C (marked in red colour), respectively.

In order to further determine the influence of the phase stabilization on dielectric properties, the ε'-T curves of each sample were measured in the temperature range of 25~450 ºC, as shown in **Figure 4a**. **Fig. 4a** shows the temperature dependence of the dielectric permittivity ε´ (at 50 kHz) of KNL−$(NTS)_{1-x}W_{5x/6}$ ceramics as a function of x. These curves present two transitions with temperature. The first one, near room temperature, is associated to the orthorhombic-tetragonal phase transition (T_{O-T}), while the second one, at 280±5ºC, corresponds to the ferroelectric–paraelectric phase transition (Curie temperature, T_C). Considering the results of both XRD patterns and ε'-T curves [See **Figs. 1** and **4(a-b)**], we can deduce that all samples belong to orthorhombic (O) and tetragonal (T) phase coexistence.[24-26] It is also known that in (K,Na,Li)(Nb,Ta)O_3 ceramics, the orthorhombic–tetragonal phase transition temperature, T_{O-T}, decreases as a result of the Li^+ addition, which stabilizes the tetragonal symmetry.[33] Previous studies have shown that the doping with Mo^{6+}, Ni^{2+}, or Mn^{2+} increases T_{O-T} in KNN.[34, 32, 35] The observed shifts in the T_{O-T} indicate that the W^{6+} incorporation into the perovskite structure promotes the stabilization of the orthorhombic symmetry at room temperature, as can be observed by X-ray diffraction, due to the secondary phase formation which partially retains the alkaline elements (Li, Na, K). Here we will also mainly focus on the variations of the T_C values as a function of W^{+6}, **Fig. 4(b).** As compared with the KNN-based ceramics

without W^{6+} we can notice that the ceramics with W^{6+} have a lower T_C. This phenomenon is consistent with previously reported results in KNN with the addition of other doping in B-site.[34-37]

In addition, some differences in the T_{O-T} and T_C peak shapes were also observed, as shown in **Fig. 4(c-d)**. The T_{O-T} peak shape of the ceramics with $0.00 \leq x \leq 0.005$ match effectively with the **T** phase of KNN and the ceramics with $0.01 \leq x \leq 0.05$ possess **O** and **T** mixed phases [see **Fig.4(c)** and **(d)**]. Moreover, we can observe from **Fig. 4(c)** and **(d)** a more frequency dependence in the ceramics with large W^{6+}content. Thus, the cause of this behaviour can be related to chemical inhomogeneities. These inhomogeneities are characteristics of polymorphism and generally appear as polar nanoregions (PNRs), which are typical in relaxor systems, or when phase's diffusion is present. As mentioned above, the doping effects on the ceramics are also reflected in the T_C transition. One can see that the ceramics with high W^{6+} contents ($x \geq 0.03$) have a larger frequency dependence and presents some characteristics of a relaxor-like behaviour[38]: *(i)* a broad maximum in the thermal dependence of the dielectric permittivity and *(ii)* a frequency dependence of the maximum of the dielectric constant (the maximum is slightly shifted to higher temperatures when the frequency is increased). Thus, this "relaxor-like" behaviour is particularly clear for the sample with high W^{6+} contents ($x \geq 0.03$) (**Fig. 4d**) and seems to disappear for the undoped ceramic (**Fig. 4c**).

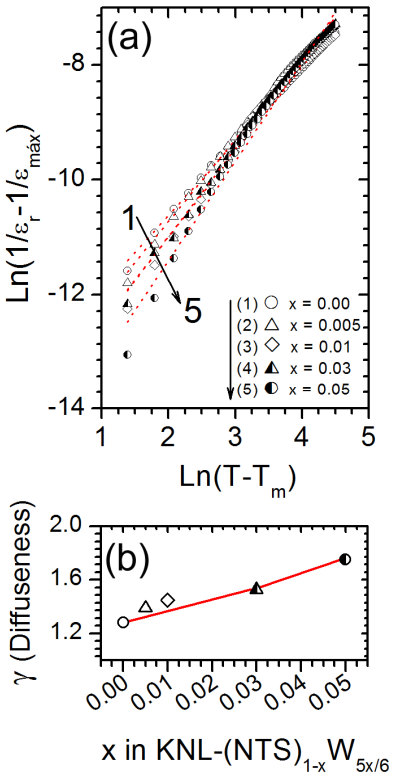

Figure 5. **(a)** Plots corresponding to the modified Curie–Weiss law for the KNL−$(NTS)_{1-x}W_{5x/6}$ sintered ceramics. The symbols denote experimental data, while the red dot lines correspond to the least-squares fitting of the modified Curie–Weiss law. **(b)** Diffuseness, γ, of the ceramics as a function of the W^{6+} content

To verify such behaviour, the diffuseness of the phase transition can be determined from the modified Curie-Weiss law, $1/\varepsilon' - 1/\varepsilon_m = C^{-1}(T-T_m)^{\gamma}$ [38] for which $\gamma = 2$ corresponds to a relaxor behaviour while $\gamma = 1$ corresponds to a classical ferroelectric–paraelectric phase transition.[39] **Figure 5(a)** shows the plots of $\ln(1/\varepsilon' - 1/\varepsilon_m)$ vs $\ln(T-T_m)$ of the KNL−$(NTS)_{1-x}W_{5x/6}$ ceramics for different W^{6+} amounts and sintered at 1125 °C for 2 hours. All the samples exhibit a linear relationship. The γ value was determined by least-squares fitting of the experimental data to this modified Curie-Weiss law, **Fig. 5(b)**. For the ceramics with $x = 0.00$, the γ value calculated is 1.27, suggesting a normal ferroelectric behaviour. As W^{6+} content increases, γ intensifies gradually, **Fig. 5(b),** reaching a value of 1.75 for the ceramics with $x = 0.05$, indicating that the ceramic has been evolved from a normal ferroelectric state toward a "relaxor" state. It is suggested that this behaviour is due to the cation disorder in the perovskite unit cell and the consequent micro domain formation.[40] Such disorder and clusters are presented in PZT because solid solutions tend to have compositional fluctuations.[41-43] Thus, the combination of the XRD, CMR, FE-SEM and ε'-T curves allows us to infer that the large variations in γ values are a consequence of the appearance of the secondary phase, which provokes an increase in the local chemical heterogeneity of the system.

Following the above analysis, it is clear that the addition of W^{6+} has induced a spontaneous normal tetragonal to relaxor orthorhombic ferroelectric phase transformation. This kind of phase transition behaviour may be accompanied by the corresponding change of domain switching behaviour and domain morphology. Electric field-induced polarization hysteresis loops were measured at room temperature for the KNL−$(NTS)_{1-x}W_{5x/6}$ ceramics with x between 0.00 to 0.05 are shown in **Figure 6**. A saturated square hysteresis loop was observed for the sample with low W^{6+} concentration ($x \leq 0.01$), showing a relatively large spontaneous polarization (P_s) and remnant polarization (P_r). This is a typical characteristic of the phase that contains long-range interaction between dipoles and owns micron-sized ferroelectric domain state,[44,45] indicating that KNL−$(NTS)_{1-x}W_{5x/6}$ ceramics with low W^{6+} content belongs to a normal ferroelectric. With an increase in the W^{+6} content, the loops become much slimmer, especially for the $x = 0.05$ sample with an orthorhombic "relaxor" state. Compared to the P_r value, the saturated polarization (P_{max}) for the sample with $x = 0.05$ is only slightly less than the value of samples with a low W^{6+} concentration ($x \leq 0.01$). The results indicate that the polarization of orthorhombic phase can be aligned to the saturated state, but cannot be maintained when the applied electric field is removed. The relaxor behaviour of ferroelectrics is generally considered to originate from the local order–disorder of the crystal structure which causes the formation of PNRs and a local electric field, owing to the heterovalent occupation of B-site on the perovskite structure by W^{6+} ions. The presence of the random field can hinder the long-range dipole alignment and thus suppress the ferroelectric interaction, resulting in a lower P_s value. Although the normal ferroelectric state with long-range dipoles in a relaxor state can be excited by an electric field (i.e., larger P_{max}),[46] yet it cannot be maintained after the external electric field is released. As a result, the

sample finally exhibits a lower P_r. In addition, it is also believed that the absence of long-range dipoles restricts not only the polarization, but also tends to induce the formation of polar nanodomains.[47]

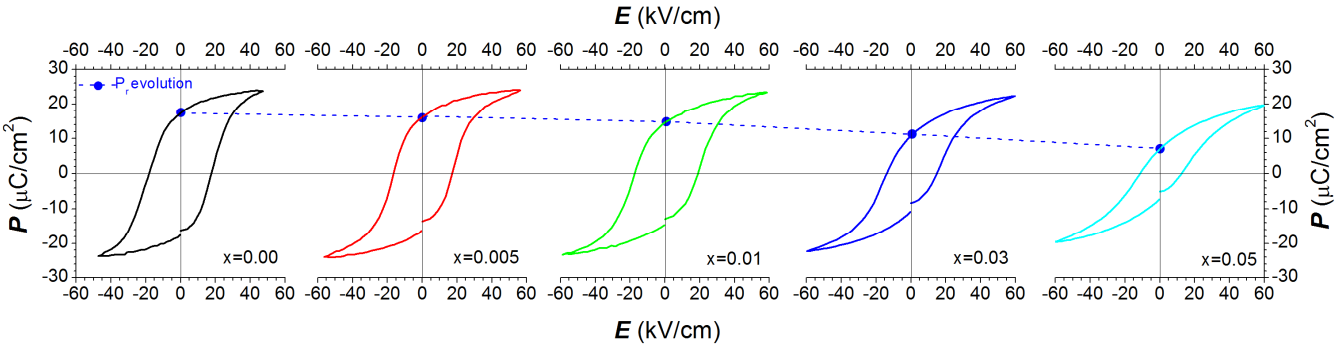

Figure 6 | Ferroelectric behaviours of the KNL−(NTS)$_{1-x}$W$_{5x/6}$ ceramics: *P–E* loops of the ceramics as a function of the *x*. The blue dot line shows the evolution of the remnant polarization (P_r). The ceramic compositions represented in (a) are the following: (**1**) x = 0.00; (**2**) x = 0.005; (**3**) x = 0.01; (**4**) x = 0.03; and (**5**) x = 0.05.

For ferroelectric materials, doping elements can act in various ways: (*i*) they can be incorporated into the structure, which is thus modified, i.e. intrinsic effects, (*ii*) they can modify the sintering and grain growth mechanisms, thus changing the microstructure (grain size, morphology) and the ferroelectric domains configuration and size, i.e. extrinsic effects and (*iii*) they can induce structural defects (like oxygen vacancies) thus modifying the pinning of ferroelectric domains. As a consequence, the role of the doping elements appears as quite complex and must be considered carefully. The ac conductivity analysis can allow us to identify the possible conduction mechanisms, and their variation with the frequency, beside it can specify us if its origin is intrinsic or extrinsic. Thus, from the imaginary part of permittivity ε´´ values at different frequencies (f), the ac conductivity (σ_{ac}) data can be calculated according to the following equation:

$$\sigma_{ac} = \varepsilon'' \bullet \varepsilon_0 \bullet \omega \quad (1)$$

where $\varepsilon_0 = 8.85 \bullet 10^{-12}$ F/m and $\omega = 2.\pi.f$. As a result, it can be observed that σ_{ac} clearly depends on the W^{6+} concentration, **Figure 7**. At high frequencies ($f \geq 10^5$ Hz) the ac conductivity slightly increased with doping, which are associated with intrinsic effects. This fact clearly shows that the solubility of W^{6+} acting as donor dopant in the B-sites position of the perovskite is very limited, in agreement with the structural results.

At low frequencies ($f \leq 10^5$ Hz), the doped ceramics exhibits a significant increase in ac conductivity of ~1 order of magnitude compared to the undoped sample, which is associated with extrinsic effects. As a logical consequence, the explanation of this evolution is that the solubility limit of the doping element is quickly reached and that excess W^{6+} ions together with some alkaline cations generate a liquid phase that enhances the formation of a secondary phase (*extrinsic effect*), as evidenced in **Figs. 2** and **3**. This secondary phase is preferably located at grain boundaries and/or triple point, and it seems to be the responsible for the grain refinement as an indication of their liquid nature during the sintering step.

Moreover, the secondary phase possesses a low crystallinity and only large amounts result in the appearance of crystallized phase. The evidence of the secondary phase presence is here demonstrated by the Confocal Raman Microscopy (**Fig. 2**), and as second evidence the ac conductivity is valuable to determine this fact. To sum up, excess W^{6+} ions promote the appearance of such secondary phase and the displacement of the alkaline equilibrium that it is also translated in small grains. The general approach to consider XRD pattern as the proof of perovskite purity is here demonstrated to be not valid enough and resembles that the presence of secondary amorphous phase is a main parameter to determine the obtaining of lower piezoelectric properties in (K,Na)NbO_3-based lead-free piezoceramics. In addition the diversity of piezoelectric properties of this system could be explained in part by the fact that the amorphous secondary phase is not well understood. Thus, higher piezoelectric properties in (K,Na)NbO_3-based lead-free piezoceramics will be obtain after careful control and reduction of the secondary phase.

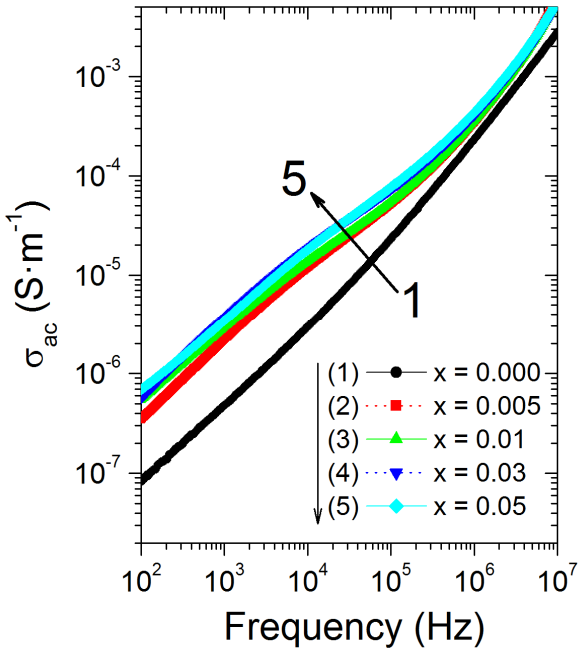

Figure 7. Plots corresponding to the ac conductivity (σ_{ac}) versus frequency of KNL−$(NTS)_{1-x}W_{5x/6}$ sintered at room temperature.

3.5. Role of the secondary phase in cationic displacement of the alkali ions forming the perovskite structure.

To verify that the secondary phase formation plays a relevant role in partial retention of the alkaline elements (Li, Na, K) forming the KNL−$(NTS)_{1-x}W_{5x/6}$ perovskite structure, additional experiments were performed by atomic force microscope (AFM) and CRM. The ceramic with higher W^{6+} contents, x = 0.05, was chosen to set at which the secondary phase concentration was maximized. **Figure 8(a)** depicts an optical microscopy image of the sample with x = 0.05 aligned

perpendicularly to the AFM cantilevers. The area of 14 × 14 μm (**Fig. 8a**) delimits the range where topographic information was collected by AFM. **Fig. 8(b.1)** shows a detailed AFM topographic image of two grains corresponding to the secondary phase structure with plate-like shape. The AFM scans along the white arrow of **Fig 8(b.1)** is illustrated in **Fig. 8(b.2)**. The grain associated with the secondary phase (i) has a grain size of ~ 4 μm and (ii) at close to grain boundary appears protrusions (height difference of ~400 nm).

CRM is here combined with AFM in the same experimental setup, thus giving direct correlations between topography and local structure. The selected area is the one previously studied by AFM. Raman spectra having same Raman shift are classified by the colours and colour intensity corresponds to the Raman intensity, such as we show in **Figs. 2**. The colour combination results in (*i*) Raman image of the surface (**Fig. 8c.1**) and (*ii*) Raman depth scan image of the cross-section (**Fig. 8c.2**). From these results we can deduce that there is a clear correlation between the secondary phase region (marked in blue colour) and the protrusion evidenced by AFM. This phenomenon results from the partial retention of the alkali elements (Li, Na, K) induced by the secondary phase formation at high temperatures during the sintering step, which promotes the displacement of the alkaline elements from the main KNL-NTS phase (red region in **Figs. 6c1-2**) to the new secondary phase (blue region in **Figs. 8c1-2**). As a consequence, we can conclude that the partial retention of the alkaline elements (Li, Na, K) onto the secondary phase, plays an important role in the increase of T_{O-T} and the simultaneous decrease of T_C in KNL-NTS phase, as shown in **Figs. 4**.

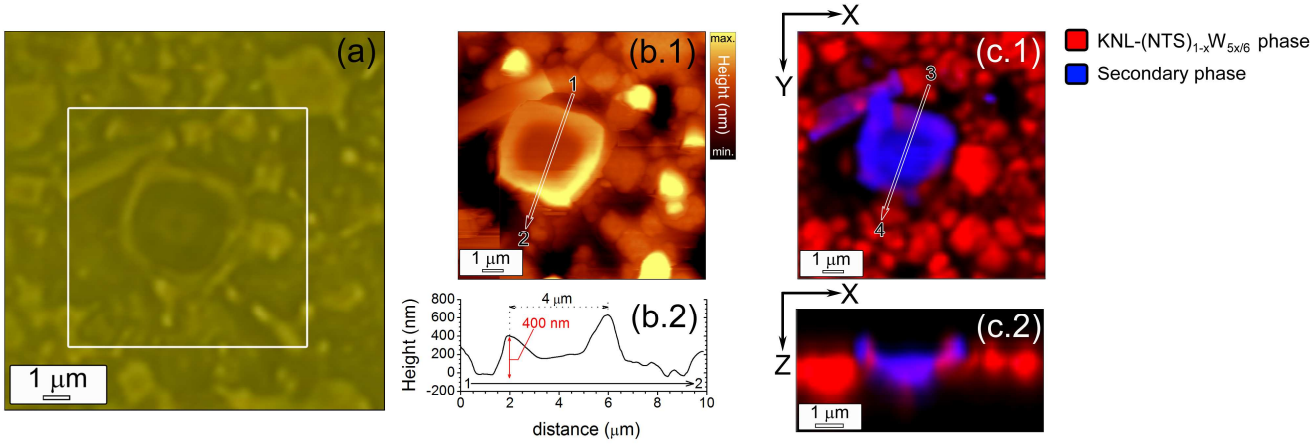

Figure 8. (a) Optical micrograph of the polished surface and thermally etched of the KNL−$(NTS)_{1-x}W_{5x/6}$ sintered ceramics with x= 0.05. **(b.1)** AFM image of KNL−$(NTS)_{1-x}W_{5x/6}$ sintered ceramics with x= 0.05, showing the topography of the secondary phase inside the marked white box of (a). **(b.2)** AFM topography scans along the white arrow of (b.1). The white rectangle in the panel (a) shows the positions where the *XY* Raman image is performed and corresponds with the area of previous AFM analysis. The Raman image shows the secondary phase distribution (blue regions) at the surface by colour code **(c.1)** as well as in the depth scan **(c.2).** The white arrow in the panel (c.1) shows the position where the *XZ* Raman depth scans image is performed.

4. Conclusions

$(K_{0.44}Na_{0.52}Li_{0.04})[(Nb_{0.86}Ta_{0.10}Sb_{0.04})_{1-x}W_{5x/6}]O_3$ lead-free piezoceramics have been prepared by solid state reaction, and the effects of the W^{6+} content on their phase structure, microstructure, and electrical properties were investigated in detail. The replacement in the B (Nb^{+5}, Ta^{+5} and Sb^{+5}) sites of the perovskite lattice resulted in the presence of a polymorphic behaviour between a **T** symmetry and an **O** symmetry onto the perovskite structure, and in the formation of a new secondary phase. Moreover, the partial retention of the alkaline elements (Li, Na, K) onto the secondary phase provokes the increase of T_{O-T} and the simultaneous decrease of T_C in KNL.NTS. Both structural features can be modified by the W^{6+} content, resulting in the tuning of the phase transitions of the system. Thus, it is worth noting that the ceramics with higher W^{6+} content develops a high diffusivity value (γ) that it can be explained as a consequence of an increase in the local chemical heterogeneity of the system. As a result, we believe that the significance of this work lies in the understanding of the structural effects caused by the dopants addition on $(KNa)NbO_3$-based lead-free ceramics, and hence this knowledge can lead to the expanding of their applications range.

5. Acknowledgments

The authors are grateful to CONICET, ANPCyT (Argentina) and MICINN project MAT2013-480089-C04-1-P for the financial support provided for this research. Dr. F. Rubio-Marcos is also indebted to MINECO for a ''Juan de la Cierva'' contract (ref: JCI-2012-14521), which is cofinanced with FEDER funds.

References

1 J. Rodel, W. Jo, K.T.P. Seifert, E.M. Anton, T. Granzow and D. Damjanovic*, J. Am. Ceram. Soc.,* 2009,**92**, 1153−1177.

2 K. Wang, J. Li and N.F. Liu, *Appl. Phys. Lett.,* 2008*,* **93**, 092904.

3 J. Wu, Y. Wanga and H. Wang, *RSC Adv.*, 2014, **4**, 64835-64842.

4 J. Wu, *RSC Adv.*, 2014, **4**, 53490-53497.

5 L-Q. Cheng, K. Wang, J-F. Li, Y. Liu and J. Li, *J. Mater. Chem. C*, 2014, **2**, 9091-9098

6 S.J. Zhang, R. Xia, H. Hao, H.X. Liu and T.R. Shrout, *Appl. Phys. Lett.,* 2008, **92**, 152904.

7 Y. Guo, K. Kakimoto and H. Ohsato, *Appl. Phys. Lett.*, 2008, **85**, 04121.

8 Z.P. Yang, Y.F. Chang and L.L. Wei, *Appl. Phys. Lett.,* 2007, **90**, 042911.

9.- J. Wu and Y. Wang, *Dalton Trans.*, 2014, **43**, 12836-12841.

10 A. Thongtha and T. Bongkarn, *Key Engineering Materials,* 2011, **474−476**, 1754−1759.

11 H. Wang, R. Zuo, Y. Liu and J. Fu, *J. Mater. Sci.*, 2010, **45**, 3677-3682.

12 D. Maurya, A. Pramanick, M. Feygenson, J. C. Neuefeind, R. J. Bodnar and S. Priya, *J. Mater. Chem. C*, 2014, **2**, 8423-8431.

13 Y.-J. Dai, X.-W. Zhang and K.-P. Chen, *Appl. Phys. Lett.*, 2009, **94**, 042905.

14 Y. Saito, H. Takao, T. Tani, T. Nonoyama, K. Takatori, T. Homma, T. Nagaya and M. Nakamura, *Nature*, 2004, **432**, 84–87.

15 J. Venkatesh, V. Sherman, and N. Setter, *J. Am. Ceram. Soc.,* 2005, **88**, 3397–3404.

16 X. Vendrell, J.E. García, F. Rubio-Marcos, D.A. Ochoa, L. Mestres and J.F. Fernández, *J. Eur. Ceram. Soc.,* **33**, 825−831.

17 D.A. Ochoa, J.A. Garcia, R. Perez, V. Gomis, A. Albareda, F. Rubio-Marcos, J.F. Fernandez, *J. Phys. D: Appl. Phys.,* 2009, **42**, 025402.

18 G.-Z. Zang, L.-B. Li, X.-J. Yi, J. Du, and Y. Li, *J Mater Sci: Mater Electron*., 2012, **23**, 977–980.

19 Jyoti Rani, K.L. Yadav, and Satya Prakash*, Materials Science and Engineering B,* 2013, **178**,1469–147.

20 R.D. Shannon, *Acta Crystallogr.,* 1976, ***A32***, 751−767.

21 F. Rubio-Marcos, P. Marchet, T. Merle-Méjean, J.F. Fernandez, *Mater. Chem. Phys.,* 2010, **123**, 91−97.

22 L. Ramajo, J. Taub and M.S. Castro, *J. Mater. Sci.: Mater. Electron*. 2014, **25**, 168−173.

23 J. Rödel, W. Jo, K. T. P., Seifert, E. M. Anton, T. Granzow, D. Damjanovic, *J. Am. Ceram. Soc.* 2009, **92**, 1153−1177.

24 F. Rubio-Marcos, J.J. Romero, M.S. Martín-Gonzalez and J.F. Fernández, *J. Eur. Ceram. Soc.,* 2010, **30**, 2763−2771.

25 L. Ramajo, M. Castro, F. Rubio-Marcos and J. Fernandez-Lozano, *J. Mater. Sci.: Mater. Electron.,* 2013, **24**, 3587−3593.

26 F. Bortolani, A. del Campo, J.F. Fernandez, F. Clemens and F. Rubio-Marcos, Chem. Mater*.,* 2014, **26**, 3838−3848.

27 Y. Shiratori, A. Magrez and C. Pithan, *Chem. Phys. Lett.,* 2004, **391**, 288−292.

28 K. Kakimoto, K. Akao, Y.P. Guo and H. Ohsato, *Jpn. J. Appl. Phys*., 2005, **44**, 7064.

29 Y. Wang, D. Damjanovic, N. Klein and N. Setter, *J. Am. Ceram. Soc.,* 2008, **91**, 1962−1970.

30 F. Rubio-Marcos, A. del Campo, R. López-Juárez, J.J. Romero and J.F. Fernández, *J. Mater. Chem.,* 2012, **22**, 9714−9720.

31 L. Ramajo, F. Rubio-Marcos, A. del Campo, J.F. Fernandez, M.S. Castro and R. Parra, *Ceram. Int.,* 2014, **40**, 14701−14712.

32 F. Rubio-Marcos, P. Marchet, J. Romero and J.F. Fernández, *J. Eur. Ceram. Soc.,* 2011, **31**, 2309−2317.

33 E. Hollenstein, M. Davis, D. Damjanovic and N. Setter, *Appl. Phys. Lett.,* 2005, **87,** 182905.

34 L. Ramajo, M. Castro, A. del Campo, J.F. Fernandez and F. Rubio-Marcos, *J. Eur. Ceram. Soc.,* 2014, **34**, 2249−2257.

35 F. Rubio-Marcos, P. Marchet, X. Vendrell, L. Mestres, J.J. Romero, R. Rémondiere, J.F. Fernández., *J. Alloy. Compd.,* 2011, **509**, 8804−8811.

36 E. Li, H. Kakemoto, S. Wada and T. Tsurumi, *J. Am. Ceram. Soc.,* **90**, 1787−1791.

37 E.M. Alkoy and M. Papila, *Ceram. Int.,* 2010, **36**, 1921−1927.

38 L.E. Cross, *Ferroelectrics*, 1987, **76**, 241−267.

39 G.A. Smolensky, *J. Phys. Soc. Jpn. Suppl,*. 1970, **28**, 26−37.

40 Y. Chang, Z. Yang, L. Wei and B. Liu, *Mater. Sci. Eng. A,* **437**, 301−305.

41 S.K. Saha and D.C. Agrawal, Am. Ceram. Soc. Bull., 1992,**71**, 1424−1428.

42 M. Kosec, V. Bobnar, M. Hrovat, J. Bernard, B. Malic and J. Holc, *J. Mater. Res.,* 2004, **19**, 1849−1854.

43 J.E. Garcia, D.A. Ochoa, V. Gomis, J.A. Eiras, R. Pérez, *J. Appl. Phys.,* 2012, **112**, 014113.

44 R. Zuo, J. Fu, S. Lu, and Z. Xu, *J. Am. Ceram. Soc.*, 2011, **94**, 4352–4357.

45 V. Koval, C. Alemany, J. Briancin, H. Brunckova, and K. Saksl, *J. Eur. Ceram. Soc.*, 23, 1157–1166.

46 X. H. Zhao, W. G Qu, H. He, N. Vittayakorn, and X. L. Tan, *J. Am. Ceram. Soc*., 2006, **89**, 202–209.

47 J. Ricote, R. W. Whatmore, and D. J. Barber, *J. Phys. Condens. Matter*, 2000, **12**, 323–337.